2024 IEEE/RSJ International Conference on Intelligent Robots and Systems (IROS)
October 14-18, 2024. Abu Dhabi, UAE

CATOA: Cooperative Calibration of Timestamp Measurements for Distributed Multi-Robot Localization

Feiyang Wen*, Hanying Zhao*, Jincheng Yu*, Shulin Cui†, and Yuan Shen*‡
* Beijing National Research Center for Information Science and Technology (BNRist)
Department of Electronic Engineering, Tsinghua University
† Beijing Sankuai Online Technology Co., Ltd
‡ Shanghai AI Laboratory

***Abstract*— Ultra-wideband (UWB) is a popular technology for robotic localization in global positioning system (GPS)-challenged and vision-obstructed scenarios. In UWB localization systems, distance information is extracted from ToA and ToD timestamp measurements. However, these measurements are easily influenced by hardware limitations and complex propagation environments, making an effective calibration method crucial for achieving high-accuracy ranging. This paper proposes a cooperative timestamp calibration method, which effectively mitigates ranging errors with scalability, adaptability, and flexibility. Our approach reduces the calibration complexity from $O(N^2)$ to $O(N)$ for networks within N nodes and allows for distributed implementation to lower communication costs. The enabler is developing a new timestamp measurement model that can rectify all timestamps across different devices in a unified manner, coupled with the introduction of cooperative model training techniques that accommodate both feasible and infeasible scenarios for precisely labeling node positions. Real-world experimental results show that our method reduces the ranging error from 38.02 cm to 8.17 cm within a fully labeled 4-node network and from 16.77 cm to 9.61 cm in an 8-node network without labeling.**

I. Introduction

The capability of robots to accurately determine and comprehend their spatial location within an environment is crucial for effective navigation, coordination, and swarm intelligence [1]–[3]. Ultra-wideband (UWB) localization technology emerges as a viable solution when global positioning system (GPS) is unreliable, which can deliver centimeter-level localization services [3]–[6] by performing high-accuracy ranging. However, the accuracy of UWB ranging is susceptible to hardware limitations and complex propagation environments [7]–[11]. Therefore, the development and implementation of effective calibration strategies are crucial for maintaining the precision and reliability of UWB-based localization systems.

As shown in Fig. 2(a), in UWB localization systems, transceivers measure time of arrival (ToA) and time of departure (ToD) timestamps, which are further converted into time of flights (ToFs) for ranging. UWB ranging errors typically fall into two main categories: "clock-induced" timestamp errors and "channel-induced" timestamp errors [12]. Clock-induced errors occur due to clock asynchronism among UWB devices [13] and can be mitigated by an appropriate ranging protocol [3], [14], [15]. Channel-induced errors stem from propagation factors such as multipath effects, non-line-of-sight (NLOS) conditions [7], signal distortion, antenna delays [9], and uncertainties in electronic circuits [10], [12], among others. The channel-induced errors are difficult to mitigate, since they distort raw timestamps in a non-descriptive way.

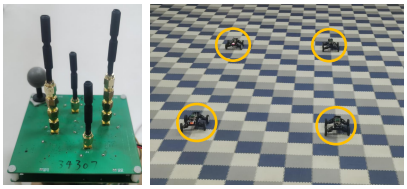

Fig. 1. (Left) UWB hardware; (Right) Scenario of real-world experiments.

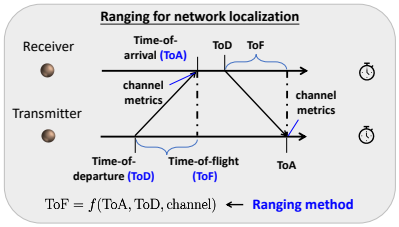

(a)

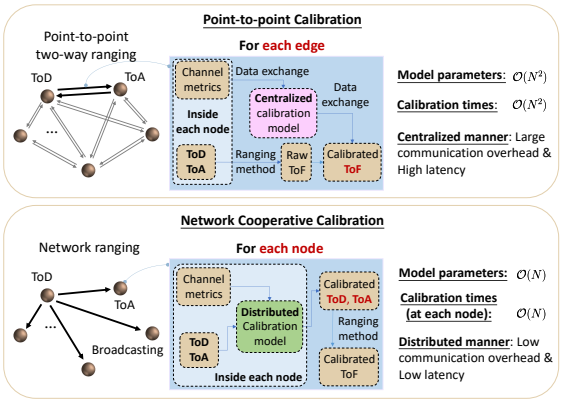

(b)

Fig. 2. (a) The relationships among ToD, ToA, and ToF. (b) Illustrations of the distinctions between current calibration methods and our method.

This paper presents CATOA, a cooperative calibration method designed to mitigate timestamp errors induced by UWB channels. This method **is scalable to swarm size, minimizes the need for manual labeling, and is independent of specific ranging algorithms**. The key to this approach is the development of a novel error model that enables rectifying all ToA measurements across different devices through a single,

unified model and facilitates the network calibration performed cooperatively. In this way, we significantly improve the computing efficiency, reduce the storage and communication burden, and make the calibration method independent of specific ranging algorithms. Moreover, CATOA allows for efficient training from a cold start, enabling the determination of model parameters without the need for manual labeling of the true positions of devices. Real-world experimental results show that CATOA effectively mitigates ranging errors.

II. Related works

Previous research has demonstrated various attempts to mitigate channel-induced errors. In [10], [11], the authors propose to relate the ToF estimation error with the power level of the received signal through a lookup table and spline fit. Similarly, [16] propose to estimate ranging errors by using a linear model based on the actual distance and the received signal strength. Alternatively, [17] and [18] model range measurements as a Gaussian process with respect to the poses of the antennas, while the authors of [19] estimate ranging errors through a Gaussian mixture model (GMM). In [7] and [8], the mitigation of ranging biases is achieved through a support vector machine (SVM), where channel parameters including Energy, Maximum amplitude and Rise time are selected as the input features. In [9] and [20], the authors estimate ranging errors from the channel impulse response (CIR) via deep learning models. The above works contribute to advancing the understanding and mitigation of UWB ranging errors. However, scalability, adaptability, and flexibility of these methods remain a challenge:

*1) **Scalability**:* The characteristics of channel-induced errors vary across different UWB modules. Existing methods often use distinct model parameters for each UWB module pair. Thus the calibration times (i.e., calibration complexity) increase quadratically with the network scale, restricting the practicality in large-scale deployments.

*2) **Adaptability**:* Current approaches commonly calibrate ranging/localization errors. By doing so, changes in the ranging/localization method often require complete revisions of the calibration parameters, impinging on the adaptability to accommodate different systems.

*3) **Flexibility**:* Previous methods need to collect signal characteristics from other nodes for calibration, which will lead to a heavy communication burden. This requirement impedes the feasibility of distributed calibration and further hinders the overall flexibility of the localization process.

To address the above challenges, we propose CATOA that cooperatively calibrates channel-induced timestamp errors with scalability, adaptability, and flexibility.

III. Preliminary

A. Problem Formulation

Consider a localization network with N robots. Assume that the j-th ranging signal is received by node i at true time $t_j^{(i)}$. According to the IEEE 802.15.4a standard, the timestamp measurement $\mathsf{t}_j^{(i)}$ can be described by

$$\mathsf{t}_j^{(i)} = \mathsf{k}^{(i)} t_j^{(i)} + \theta^{(i)} + \mathsf{w}_j^{(i)} \tag{1}$$

where $\mathsf{k}^{(i)}$ and $\theta^{(i)}$ characterize the effect of clock skew and clock boot time, respectively, and $\mathsf{w}_j^{(i)}$ denotes the channel-induced measurement error. In this paper, we focus on mitigating $\mathsf{w}_j^{(i)}$, whereas the clock-induced errors $\mathsf{k}^{(i)}$ and $\theta^{(i)}$ are mitigated using signal-multiplexing network ranging (SM-NR), which is our previous work presented in [3]. While our calibration approach is derived using SM-NR, **it operates independently from any specific ranging method**.

In SM-NR, each node emits a ranging signal in sequence. Then, the first-transmission node transmits a signal again to end the ranging period. Assume that the j-th ranging signal is transmitted by node j. An estimation of the ToF $\hat{\mathsf{T}}_{i,j}$ between nodes i and j that mitigates clock-induced errors is given by SM-NR according to [3]. Let $\boldsymbol{p}^{(n)}$ denote the position of the n-th node. Then the exact ToF value between nodes i and j is given by $T_{i,j} = \|\boldsymbol{p}^{(i)} - \boldsymbol{p}^{(j)}\|/c$, where c denotes the speed of signal. It can be verified that

$$\hat{\mathsf{T}}_{i,j} - T_{i,j} \approx \big[(\mathsf{w}_j^{(i)} - \mathsf{w}_i^{(i)}) - (\mathsf{w}_j^{(j)} - \mathsf{w}_i^{(j)})\big]/2, \tag{2}$$

where $\mathsf{w}_j^{(i)}$ requires further calibration efforts.

B. Gaussian Process Regression

CATOA uses the scalable variational Gaussian process (SVGP) to model channel-induced errors, which is a variant of the Gaussian process regression (GPR) with lower computational complexity on large datasets [21]–[23].

Consider a training dataset consisting of D input vectors $\boldsymbol{X} = [\boldsymbol{x}_1, \boldsymbol{x}_2, \cdots, \boldsymbol{x}_D]$ and corresponding observed targets $\mathbf{y} = [\mathsf{y}_1, \mathsf{y}_2, \cdots, \mathsf{y}_D]^{\mathrm{T}}$. Suppose that $p(\mathbf{y}|\mathbf{f}) = \mathcal{N}\left(\mathbf{y}|\,\mathbf{f}, \sigma^2 \boldsymbol{I}\right)$, where σ is a hyperparameter denoting the observation noise, and $\mathbf{f} = [\mathsf{f}_1, \mathsf{f}_2, \cdots, \mathsf{f}_D]^{\mathrm{T}}$ with a latent function $\mathsf{f}_i = f(\boldsymbol{x}_i)$. To reduce the computational cost, the SVGP framework introduces a set of *inducing points* $\boldsymbol{Z} = [\boldsymbol{z}_1, \boldsymbol{z}_2, ..., \boldsymbol{z}_M]^{\mathrm{T}}$ and *inducing variables* $\mathbf{u} = [\mathsf{u}_1, \mathsf{u}_2, ..., \mathsf{u}_M]^{\mathrm{T}}$ with $M \ll D$, and assumes the following joint prior distribution:

$$p(\mathbf{f}, \mathbf{u}) = \mathcal{N}\left(\begin{bmatrix}\mathbf{f}\\ \mathbf{u}\end{bmatrix} \middle|\, \mathbf{0}, \begin{bmatrix}\boldsymbol{K}_{\mathrm{D}} & \boldsymbol{K}_{\mathrm{DM}}\\ \boldsymbol{K}_{\mathrm{DM}}^{\mathrm{T}} & \boldsymbol{K}_{\mathrm{M}}\end{bmatrix}\right) \tag{3}$$

where $[\boldsymbol{K}_{\mathrm{D}}]_{d_1 d_2} = k(\boldsymbol{x}_{d_1}, \boldsymbol{x}_{d_2}; \boldsymbol{\theta})$, $[\boldsymbol{K}_{\mathrm{DM}}]_{dm} = k(\boldsymbol{x}_d, \boldsymbol{z}_m)$, $[\boldsymbol{K}_{\mathrm{M}}]_{m_1 m_2} = k(\boldsymbol{z}_{m_1}, \boldsymbol{z}_{m_2})$, in which $k(\cdot, \cdot; \boldsymbol{\theta})$ is a kernel function with hyperparameter $\boldsymbol{\theta}$.

To approximate the posterior distribution of $\mathbf{u}$, a variational distribution $q(\mathbf{u}) = \mathcal{N}(\mathbf{u}|\,\boldsymbol{m}, \boldsymbol{S})$ is introduced. Then, we can derive a variational lower bound of the marginal likelihood $\log p(\mathbf{y}) \geq \mathcal{L}$. The analytical form of $\mathcal{L}$ is presented in [21]. During the training phase, the variational variables $\boldsymbol{Z}, \mathbf{u}$ and the hyperparameters $\boldsymbol{\theta}, \sigma$ are determined by maximizing $\mathcal{L}$.

During the reference phase, given a new input $\boldsymbol{x}_{\mathrm{P}}$, the predictive distribution yields $p(\mathsf{y}_{\mathrm{P}}|\boldsymbol{x}_{\mathrm{P}}) = \mathcal{N}(\mathsf{y}_{\mathrm{P}}|\,\mu_{\mathrm{P}}, \sigma_{\mathrm{P}}^2 + \sigma^2)$, where $\mu_{\mathrm{P}} = \boldsymbol{a}\boldsymbol{m}$, $\sigma_{\mathrm{P}}^2 = k(\boldsymbol{x}_{\mathrm{P}}, \boldsymbol{x}_{\mathrm{P}}) + \boldsymbol{a}(\boldsymbol{S} - \boldsymbol{K}_{\mathrm{M}})\boldsymbol{a}^{\mathrm{T}}$ in which $\boldsymbol{a} = \boldsymbol{k}_{\mathrm{PM}}\boldsymbol{K}_{\mathrm{M}}^{-1}$ with $[\boldsymbol{k}_{\mathrm{PM}}]_m = k(\boldsymbol{x}_{\mathrm{P}}, \boldsymbol{z}_m)$.

IV. A Probabilistic ToA Error Model for Cooperative Calibration

We establish a probabilistic model for ToA errors, which not only provides an estimation of the systematic bias but also quantify the variance of these errors. In this way, the

calibration results can be further incorporated into localization or filtering framework within soft information.

A. ToA Measurement Errors

1) Hardware-induced errors: These errors stem from the hardware components within the UWB modules, which include the delays induced by antennas and circuits. We introduce a node-specific parameter $o^{(i)}$ for these errors.

2) Propagation-induced errors: The ToA errors are also highly correlated with the wireless signal propagation environments, since UWB modules (DWM1000) perform the leading edge detection (LDE) algorithm to estimate the ToA from the CIR samples [10], [12]. However, directly processing raw high-dimensional CIR data is computationally expensive. Prior work [10], [16] have showed that the received signal power can effectively reflect the distortion and the multipath effect present in the received signal.

Inspired by this observation, our calibration method extracts two channel parameters from the CIR samples to reduce the input dimensions, i.e., the *received power level*

$$P_{\mathrm{R}} = 10\log_{10}\left(\sum_{i=1}^{Q}|s[i]|^2 \times 2^{17}/Q^2\right) - A_{\mathrm{R}} \tag{4}$$

and the *first path SNR*

$$P_{\mathrm{F}} = 10\log_{10}\left(F_2^2/\sigma_{\mathrm{CIR}}^2\right) \tag{5}$$

where $s[i]$ is the value of the i-th CIR sample, Q is the number of CIR samples, A_{R} is a constant determined by UWB devices, F_2 is one of the three characteristic first path amplitudes as defined in [12], and σ_{CIR} is the standard deviation of the noise level. $F_2, \sigma_{\mathrm{CIR}}$ are evaluated by the LDE algorithm [10], [12]. Based on the discussion above, we model the channel-induced ToA error $\mathsf{w}_j^{(i)}$ as[1]

$$\mathsf{w}_j^{(i)} = \boldsymbol{\zeta}(\boldsymbol{P}_j^{(i)}) + o^{(i)} \tag{6}$$

where $\boldsymbol{P}_j^{(i)} = [P_{\mathrm{R},j}^{(i)}, P_{\mathrm{F},j}^{(i)}]^{\mathrm{T}}$, $\boldsymbol{\zeta}(\boldsymbol{P}_j^{(i)})$ reflects the propagation-related errors. It is further decomposed as

$$\boldsymbol{\zeta}(\boldsymbol{P}_j^{(i)}) = \mathsf{b}(\boldsymbol{P}_j^{(i)}) + \boldsymbol{\nu}(\boldsymbol{P}_j^{(i)}) \tag{7}$$

in which b and $\boldsymbol{\nu}$ denote the systematic bias and the measurement noise, respectively. To model $\boldsymbol{\nu}$, we collect real data for analysis, as shown in Fig. 3. It is shown that the variance of $\boldsymbol{\nu}$ is also related to the signal power level. Thus we model $\boldsymbol{\nu}$ as $p(\boldsymbol{\nu}) = \mathcal{N}(\boldsymbol{\nu}|\,0, \sigma_{\mathrm{b}}^2(\boldsymbol{P}))$, where $\sigma_{\mathrm{b}}^2(\boldsymbol{P})$ denotes the variance of the observation noise.

B. ToA Measurement Error Modeling Based on SVGP

To simultaneously fit $\mathsf{b}(\boldsymbol{P})$ and estimate the input-dependent noise $\sigma_{\mathrm{b}}^2(\boldsymbol{P})$, we use two independent SVGP models to separately estimate the probability distribution of $\mathsf{b}(\boldsymbol{P})$ and $\sigma_{\mathrm{b}}^2(\boldsymbol{P})$, following [24]. For brevity, define a latent function $g(\boldsymbol{P})$ such that $\sigma_{\mathrm{b}}^2(\boldsymbol{P}) = e^{g(\boldsymbol{P})}$.

For the training of these two SVGP models, we gather data by letting UWB modules transmit signals. For simplicity

[1]When $i = j$, $\mathsf{w}_i^{(i)}$ represents the ToD measurement error, which is mainly caused by a constant transmitter antenna delay and is not related to the characteristics of the received signal [12]. Therefore, we combine it into $o^{(i)}$ and set $\mathsf{w}_i^{(i)} = 0$, which will not impair the calibration performance.

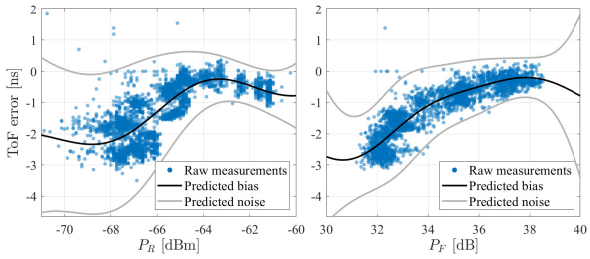

Fig. 3. The relation between ToF errors and the levels of received signal power. Since the true value of ToA is unavailable in practice, we evaluate ToF instead. The "Predicted bias" curve is $\mathsf{b}(\boldsymbol{P})$ predicated by our model, while the "Predicted noise" curve depicts $\mathsf{b}(\boldsymbol{P}) \pm 3\sigma_{\mathsf{b}}(\boldsymbol{P})$.

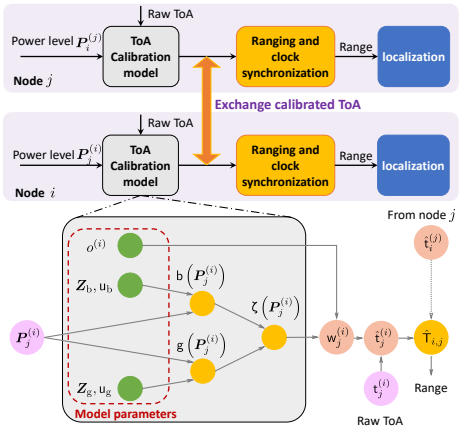

Fig. 4. The implementation process of the calibration model.

but without loss of generality, our investigation focus on **a single ranging period**. During this period, there are $N+1$ signal transmissions in total within this ranging period in a N-node network, according to the SM-NR protocol. Ideally, we will have a training dataset within received power levels $\boldsymbol{P} = [\boldsymbol{P}_1^{(1)} \cdots \boldsymbol{P}_{N+1}^{(1)}\ \boldsymbol{P}_1^{(2)} \cdots \boldsymbol{P}_{N+1}^{(N)}] \in \mathbb{R}^{2\times D}$ and a dataset with corresponding ToA measurement errors $\mathbf{w} = [\mathsf{w}_1^{(1)}\ \mathsf{w}_2^{(1)} \cdots \mathsf{w}_{N+1}^{(N)}]^{\mathrm{T}} \in \mathbb{R}^{D\times 1}$ with $D = N(N+1)$. Define $\mathbf{b} = [\mathsf{b}_1\ \mathsf{b}_2 \cdots \mathsf{b}_D]^{\mathrm{T}}$ and $\mathbf{g} = [\mathsf{g}_1\ \mathsf{g}_2 \cdots \mathsf{g}_D]^{\mathrm{T}}$, in which $\mathsf{b}_d = \mathsf{b}(\boldsymbol{P}_d)$ and $\mathsf{g}_d = \mathsf{g}(\boldsymbol{P}_d)$, with $\boldsymbol{P}_d$ being the dth column in $\boldsymbol{P}$. Two Gaussian process priors over $\mathbf{b}$ and $\mathbf{g}$ are assumed as $p(\mathbf{b}) = \mathcal{N}(\mathbf{b}|\,\mathbf{0}, \boldsymbol{K}_{\mathrm{b}})$ and $p(\mathbf{g}) = \mathcal{N}(\mathbf{g}|\,\mathbf{0}, \boldsymbol{K}_{\mathrm{g}})$, where the covariance matrices $\boldsymbol{K}_{\mathrm{b}}$ and $\boldsymbol{K}_{\mathrm{g}}$ are derived from the following kernel functions:

$$[\boldsymbol{K}_{\mathrm{b}}]_{d_1 d_2} = k_{\mathrm{b}}(\boldsymbol{P}_{d_1}, \boldsymbol{P}_{d_2}) \triangleq \exp\left[-\|\boldsymbol{P}_{d_1} - \boldsymbol{P}_{d_2}\|^2/2\theta_{\mathrm{b}}^2\right]$$
$$[\boldsymbol{K}_{\mathrm{g}}]_{d_1 d_2} = k_{\mathrm{g}}(\boldsymbol{P}_{d_1}, \boldsymbol{P}_{d_2}) \triangleq \exp\left[-\|\boldsymbol{P}_{d_1} - \boldsymbol{P}_{d_2}\|^2/2\theta_{\mathrm{g}}^2\right]$$

Following SVGP, we incorporate inducing points $\boldsymbol{Z}_{\mathrm{b}} = [\boldsymbol{z}_{\mathrm{b},1}, \boldsymbol{z}_{\mathrm{b},2}, ..., \boldsymbol{z}_{\mathrm{b},\mathrm{M}}]^{\mathrm{T}}$, $\boldsymbol{Z}_{\mathrm{g}} = [\boldsymbol{z}_{\mathrm{g},1}, \boldsymbol{z}_{\mathrm{g},2}, ..., \boldsymbol{z}_{\mathrm{g},\mathrm{M}}]^{\mathrm{T}}$ and inducing variables $\mathbf{u}_{\mathrm{b}}, \mathbf{u}_{\mathrm{g}} \in \mathbb{R}^{M\times 1}$. Distributions $q_b(\mathbf{u}_{\mathrm{b}}) = \mathcal{N}(\mathbf{u}_{\mathrm{b}}|\boldsymbol{m}_{\mathrm{b}}, \boldsymbol{S}_{\mathrm{b}})$ and $q_g(\mathbf{u}_{\mathrm{g}}) = \mathcal{N}(\mathbf{u}_{\mathrm{g}}|\boldsymbol{m}_{\mathrm{g}}, \boldsymbol{S}_{\mathrm{g}})$, are introduced for $\mathbf{b}$ and $\mathbf{g}$, respectively. The relationship among these parameters are shown in Fig. 4. Then, a variational lower bound $\mathcal{L}_{\mathbf{w}}$ for the marginal likelihood $\log p(\mathbf{w})$ can be derived following [24]. The optimization of these parameters is achieved by maximizing $\mathcal{L}_{\mathbf{w}}$.

However, the true ToA value is unknown in practice, rendering the dataset $\mathbf{w}$ inaccessible. To address this issue,

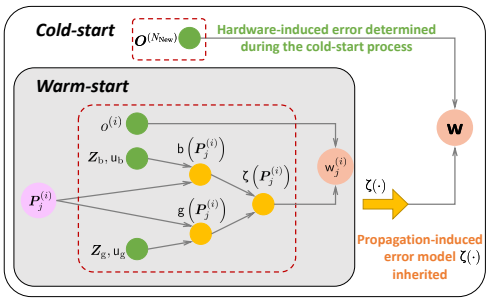

Fig. 5. The relationship between the warm-start and cold-start modes.

we present a novel training strategy, including two modes as shown in Fig. 5: the initial mode operates under the condition that the exact positions of all nodes are known for training purpose. Following this, the strategy accommodates a **cold-start** mode that enables training model parameters without the need for pre-established positions of new nodes.

C. Warm-Start: Model Training Using Full Labeling

This section presents the initial mode of our training strategy, where the exact positions of all nodes are known through pre-calibration using external techniques, such as RTK-GPS [16] or motion capture systems [18].

To substitute the unavailable ToA error dataset $\mathbf{w}$, we construct a ToF error dataset $\boldsymbol{\varepsilon}$. In one complete ranging period, using (2), the dataset $\boldsymbol{\varepsilon}$ is constructed as $\boldsymbol{\varepsilon} = \{\varepsilon_{i,j} := \hat{\mathsf{T}}_{i,j} - T_{i,j}\}_{i=1,j=i+1}^{N}$. We then derive a variational lower bound $\mathcal{L}_{\boldsymbol{\varepsilon}}$ for marginal likelihood $\log p(\boldsymbol{\varepsilon})$ based on (2):

$$\begin{aligned}\mathcal{L}_{\boldsymbol{\varepsilon}} = &\sum_{i=1}^{N}\sum_{j=i+1}^{N} \log\mathcal{N}\left(\varepsilon_{i,j}|\frac{e_j^{(i)}+e_i^{(j)}}{2}, \frac{r_j^{(i)}+r_i^{(j)}}{4}\right)\\ &-\sum_{i=1}^{N}\sum_{j=i+1}^{N}\left[\frac{1}{4}\left(\sigma_{\mathrm{g},j}^{(i)2}+\sigma_{\mathrm{g},i}^{(j)2}\right)+\frac{1}{2}\left(\frac{\sigma_{\mathrm{b},j}^{(i)2}}{r_j^{(i)}}+\frac{\sigma_{\mathrm{b},i}^{(j)2}}{r_i^{(j)}}\right)\right]\\ &-\mathrm{KL}\left[q(\mathbf{u}_\mathrm{b})||p(\mathbf{u}_\mathrm{b})\right]-\mathrm{KL}\left[q(\mathbf{u}_\mathrm{g})||p(\mathbf{u}_\mathrm{g})\right] \qquad (8)\end{aligned}$$

where $e_j^{(i)} = \mu_{\mathrm{b},j}^{(i)} + o^{(i)}$, $r_j^{(i)} = \exp(\mu_{\mathrm{g},j}^{(i)} - \sigma_{\mathrm{g},j}^{(i)2}/2)$. The detailed derivation of (8) is presented in Appendix I.

With $\mathcal{L}_{\boldsymbol{\varepsilon}}$, next, we determine the parameter $o^{(i)}$, variational variables $\boldsymbol{Z}_\mathrm{b}, \boldsymbol{Z}_\mathrm{g}, \mathbf{u}_\mathrm{b}, \mathbf{u}_\mathrm{g}, \boldsymbol{S}_\mathrm{b}, \boldsymbol{S}_\mathrm{g}$, and hyperparameters $\theta_\mathrm{b}, \theta_\mathrm{g}$ by maximizing $\mathcal{L}_{\boldsymbol{\varepsilon}}$. Following this, a model for propagation-induced ToA error $\boldsymbol{\zeta}(\boldsymbol{P})$ is established.

D. Cold-start: Model Training without External Labeling

Using external techniques to acquire position information are expensive and cumbersome. In this section, we possess a new batch of UWB modules and focus on calibrating their ranging errors without external pre-labeling, as depicted in Fig. 5. Such cold-start calibration is achieved by unleashing the benefits of node cooperation.

The positions of all new nodes are unknown but fixed. Recall (6), our approach to ToA modeling distinguishes between hardware-induced error and propagation-induced error, with the former being node-specific while the latter affecting all nodes universally. This distinction enables us to directly inherit the propagation-induced error model $\boldsymbol{\zeta}(\cdot)$, and only requiring the determination of the node-specific hardware-bias $o^{(i)}$ for new nodes. Specifically, we simultaneously estimate the positions $\boldsymbol{p} = [\boldsymbol{p}^{(1)\mathrm{T}}\ \boldsymbol{p}^{(2)\mathrm{T}}\ \cdots\ \boldsymbol{p}^{(N_\mathrm{new})\mathrm{T}}]^\mathrm{T}$ and individual biases $\boldsymbol{o} = [o^{(1)}\ o^{(2)}\ \cdots\ o^{(N_\mathrm{new})}]^\mathrm{T}$ using ranging measurements by maximizing the log-likelihood, i.e.,

$$\hat{\mathbf{p}}, \hat{\mathbf{o}} = \arg\max \log p\left(\hat{\mathbf{T}}; \boldsymbol{p}, \boldsymbol{o}\right) = \arg\min \sum_{i<j}^{N_\mathrm{new}} \frac{1}{\sigma_{i,j}^2}\left[\frac{1}{c}||\boldsymbol{p}^{(i)}-\boldsymbol{p}^{(j)}|| + \Delta T_{i,j} - \hat{\mathsf{T}}_{i,j}\right]^2. \qquad (9)$$

where $\Delta T_{i,j} = (\boldsymbol{\zeta}(\boldsymbol{P}_j^{(i)}) + \boldsymbol{\zeta}(\boldsymbol{P}_i^{(j)}) + o^{(i)} + o^{(j)})/2$ and $\sigma_{i,j}^2 = (\sigma_\mathrm{b}^2(\boldsymbol{P}_j^{(i)}) + \sigma_\mathrm{b}^2(\boldsymbol{P}_i^{(j)}))/4$. To solve the non-convex (9), we begin by initializing $o^{(i)}$ with 0 and $\boldsymbol{p}^{(i)}$ with the result of multidimensional scaling (MDS) using raw ToA measurements. Then, $\boldsymbol{o}$ and $\boldsymbol{p}$ are optimized simultaneously through gradient descent.

V. Cooperative Calibration: A Distributed Approach

As shown in Fig. 4, upon receiving a UWB signal, nodes perform ToA calibration locally. Using node i as an example for illustration, we omit the superscript $^{(i)}$ for brevity. The input power level of the received signal is denoted as $\boldsymbol{P}_\mathrm{P}$. Employing the ToA calibration model (6), we first obtain the predictive distribution of $\mathsf{b}_\mathrm{P}, \mathsf{g}_\mathrm{P}$ and then derive the distribution of propagation-induced error $\boldsymbol{\zeta}(\boldsymbol{P}_\mathrm{P})$

$$p(\boldsymbol{\zeta}|\boldsymbol{P}_\mathrm{P}) = \mathcal{N}(\boldsymbol{\zeta}|\mu_{\mathrm{b,P}}, \sigma_\mathrm{P}^2) \qquad (10)$$

where $\sigma_\mathrm{P}^2 = \sigma_{\mathrm{b,P}}^2 + \exp(\mu_{\mathrm{g,P}} + \sigma_{\mathrm{g,P}}^2/2)$, $\mu_{\mathrm{b,P}}$, $\sigma_{\mathrm{b,P}}^2$, $\mu_{\mathrm{g,P}}$, and $\sigma_{\mathrm{g,P}}^2$ take the similar form as the ones in (13) but replacing $\boldsymbol{P}_j^{(i)}$ by $\boldsymbol{P}_\mathrm{P}$. The calibrated timestamp is given by $\hat{\mathsf{t}} = \mathsf{t} - (\boldsymbol{\zeta} + o)$, which will be dispatched to other nodes for ToF and range estimation. As each node calibrates locally without acquiring additional information from other nodes, our method can be executed in a distributed manner. Thus, CATOA significantly reduces the communication overhead, increases the real-time performance, and avoids the loss of accuracy due to information aggregation.

VI. Experimental Results

To verify the performance of CATOA, we conduct experiments in real-world environments. All experiments are carried out in an indoor area measuring 50m×25m×12m. The FZMotion OptiTrack system [25] is employed to deliver accurate position data of the nodes, serving as ground truth. Each node is equipped with a four-antenna UWB array including four DWM1000 modules and a Raspberry PI for computational processes. Nodes transmit and receive UWB signals at a center frequency of 3993.6 MHz, where the DWM1000 chips provide received power data and timestamp (ToA and ToD) measurements. We concatenate the received power level from the four antennas as the input for the calibration model. Network ranging and ToA calibration are conducted on each node using the Raspberry PI.

To evaluate the effectiveness, the state-of-the-art proposed in [11] is used for performance comparison. This method employs the averaged first path power level between two nodes to model the ToF measurement error.

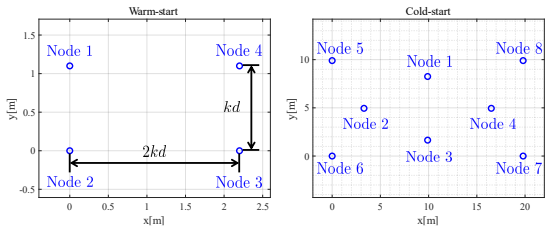

Fig. 6. Data collection for model training: (Left) Placement of four UWB modules in warm-start experiments; (Right) One of the topologies of eight UWB modules in the cold-start experiments.

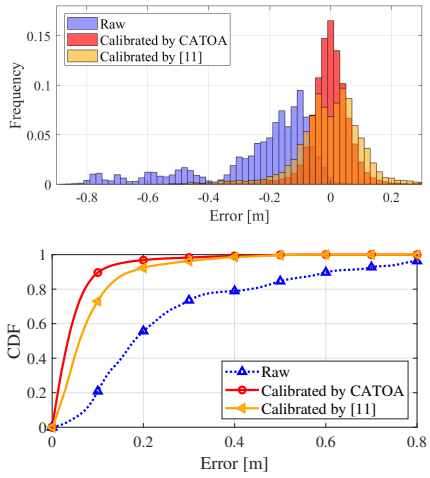

Fig. 7. The performance of the calibration model in warm-start scenarios: (Up) The ranging error histograms; (Down) The CDF of ranging error.

1) Warm-start: As shown in Fig. 6, four nodes are placed into rectangles with a fixed length-width ratio, where $d = 1.1$ m and $k = 1, 2, 3, ..., 12$. For each k, we conduct 1200 ranging periods. From these, 70% of the measurements are randomly chosen to form the training dataset, while the remaining measurements are used as the test dataset.

The calibration results on the test dataset are shown in Fig. 7. Our method achieves a root mean squared error (RMSE) of 8.17 cm, which is 78.5% better than the raw measurement with an RMSE of 38.02 cm. In comparison to the ToF-based method [11], which achieves a RMSE of 11.81 cm, our approach achieves higher accuracy, thus showing the effectiveness of our ToA error model.

2) Cold-start: We employ an additional set of 8 UWB modules to assess the cold-start training strategy in Section IV-D. As shown in Fig. 6, we firstly collect 20 ranging periods as the training dataset to determine the node-specific bias $o^{(i)}$. The propagation-induced error model ζ is inherited from the one trained on the above 4-node network. Next, we gather measurement data from 500 periods across four different topologies as the test dataset. The ranging and localization accuracy before and after calibration are evaluated, where the localization results is obtained using (9) by fixing $o^{(i)}$. For comparison, we replace ζ with the calibration model in [11] that is trained on the above 4-node network and obtain the localization results using (9).

Fig. 8 demonstrate a substantial decrease in both ranging

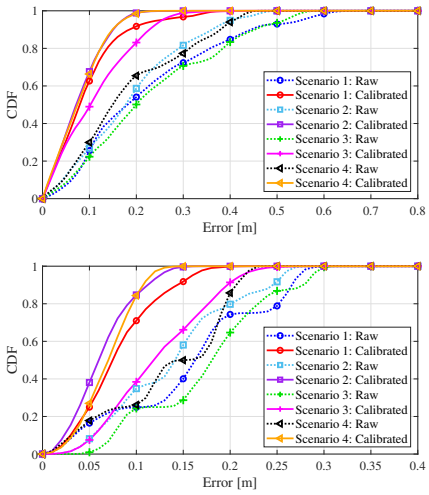

Fig. 8. The performance of the calibration model in cold-start scenarios: (Up) The CDF of ranging error; (Down) The CDF of localization error.

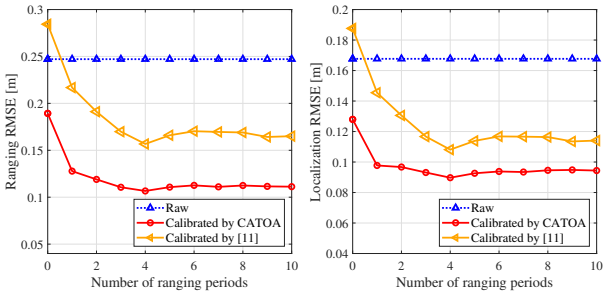

Fig. 9. Ranging and localization performance with different number of ranging periods in the training dataset of cold-start scenarios. The number of ranging periods "0" corresponds to the case where $o^{(i)}$ is not trained and is set to 0 for all nodes.

and localization errors. In particular, Fig. 8 show that the calibration model trained in one scenario can be generalized to various different scenarios, highlighting the method's effectiveness regardless of variations in network size and topology. We average RMSEs of four test scenarios. The calibrated ranging RMSE is 11.29 cm, which is 54.3% better than the raw measurements with an RMSE 24.71 cm. The calibrated localization RMSE is 9.61 cm, which also outperforms the raw RMSE, 16.77 cm, by 42.7%. In comparison, the method in [11] achieves a ranging RMSE of 16.67 cm and a localization RMSE of 11.47 cm. Moreover, we evaluate the calibration performance with different number of ranging periods in the training dataset. As shown in Fig. 9, the optimal $o^{(i)}$ can be obtained within 10 ranging periods, indicating the efficiency of cold-start training method. Hence, the cold-start training approach can significantly enhance the localization accuracy of new UWB modules without requiring heavy resource consumption.

VII. Conclusion

In this paper, we propose a novel approach to calibrating UWB ToA measurements for multi-robot localization. Specifically, we established a ToA measurement model using the received power level and the first path SNR of the received signal, and proposed the ToA calibration method

using SVGP models. We then designed the model training strategies for both feasible and infeasible external labeling. By directly calibrating the ToA measurements, the proposed method is scalable across multiple UWB devices, adaptable for different ranging methods, and can be implemented in a distributed manner with flexibility. Experimental results show that the proposed method can significantly improve the ranging and localization accuracy of UWB localization networks and exhibits strong generalizability across different network configurations.

Appendix I
Detailed Derivation of (8)

From (2), (6), we have $\boldsymbol{\varepsilon}_{i,j} = (\mathsf{w}_j^{(i)} + \mathsf{w}_i^{(j)})/2$. Then, the marginal likelihood of $\boldsymbol{\varepsilon}$ is derived as

$$p(\boldsymbol{\varepsilon}) = \int \prod_{i<j}^{N} \mathcal{N}\left(\boldsymbol{\varepsilon}_{i,j} | \frac{1}{2}\left(\mathsf{w}_j^{(i)} + \mathsf{w}_i^{(j)}\right), 0\right) p(\mathsf{w}) \mathrm{d}\mathsf{w}. \quad (11)$$

Following [24], we can analytically write $\mathcal{L}_{\mathbf{w}}$ as

$$\begin{aligned}\mathcal{L}_{\mathbf{w}} = \sum_{i\neq j}^{N} \left[\log \mathcal{N}\left(\mathsf{w}_j^{(i)} | e_j^{(i)}, r_j^{(i)}\right) - \frac{1}{4}\sigma_{\mathrm{g},j}^{(i)2} - \frac{1}{2}\frac{\sigma_{\mathrm{b},j}^{(i)2}}{r_j^{(i)}}\right] \\ - \mathrm{KL}\left[q(\mathbf{u}_\mathrm{b}) || p(\mathbf{u}_\mathrm{b})\right] - \mathrm{KL}\left[q(\mathbf{u}_\mathrm{g}) || p(\mathbf{u}_\mathrm{g})\right] \quad (12)\end{aligned}$$

where

$$\begin{aligned}&\mu_{\mathrm{b},j}^{(i)} = \boldsymbol{a}_\mathrm{b}\boldsymbol{m}_\mathrm{b}, \quad \mu_{\mathrm{g},j}^{(i)} = \boldsymbol{a}_\mathrm{g}\boldsymbol{m}_\mathrm{g} \\ &\sigma_{\mathrm{b},j}^{(i)2} = k_\mathrm{b}\big(\boldsymbol{P}_j^{(i)}, \boldsymbol{P}_j^{(i)}\big) + \boldsymbol{a}_\mathrm{b}(\boldsymbol{S}_\mathrm{b} - \boldsymbol{K}_{\mathrm{b,M}})\boldsymbol{a}_\mathrm{b}^\mathrm{T} \quad (13) \\ &\sigma_{\mathrm{g},j}^{(i)2} = k_\mathrm{g}\big(\boldsymbol{P}_j^{(i)}, \boldsymbol{P}_j^{(i)}\big) + \boldsymbol{a}_\mathrm{g}(\boldsymbol{S}_\mathrm{g} - \boldsymbol{K}_{\mathrm{g,M}})\boldsymbol{a}_\mathrm{g}^\mathrm{T},\end{aligned}$$

in which $\boldsymbol{a}_\mathrm{b} = \boldsymbol{k}_{\mathrm{b,M}}\boldsymbol{K}_{\mathrm{b,M}}^{-1}$, $\boldsymbol{a}_\mathrm{g} = \boldsymbol{k}_{\mathrm{g,M}}\boldsymbol{K}_{\mathrm{g,M}}^{-1}$, and

$$\begin{aligned}[\boldsymbol{K}_{\mathrm{b,M}}]_{m_1m_2} &= k_\mathrm{b}([\boldsymbol{z}_\mathrm{b}]_{m_1}, [\boldsymbol{z}_\mathrm{b}]_{m_2}) \\ [\boldsymbol{K}_{\mathrm{g,M}}]_{m_1m_2} &= k_\mathrm{g}([\boldsymbol{z}_\mathrm{g}]_{m_1}, [\boldsymbol{z}_\mathrm{g}]_{m_2})\end{aligned}$$

with $[\boldsymbol{k}_{\mathrm{b,M}}]_m = k_\mathrm{b}(\boldsymbol{P}_j^{(i)}, [\boldsymbol{z}_\mathrm{b}]_m)$ and $[\boldsymbol{k}_{\mathrm{g,M}}]_m = k_\mathrm{g}(\boldsymbol{P}_j^{(i)}, [\boldsymbol{z}_\mathrm{g}]_m)$. As $\log p(\mathbf{w}) \geq \mathcal{L}_{\mathbf{w}}$, the proof is completed by substituting (12) into (11) and then applying logarithms to the both sides, which yields (8).

Acknowledgment

This work was supported in part by the National Natural Science Foundation of China under Grant 62271285, in part by the National Natural Science Foundation of China under Grant 62203257, in part by Tsinghua University-Meituan Joint Institute for Digital Life, and in part by Shanghai AI Laboratory.

References

[1] M. Z. Win, Y. Shen, and W. Dai, "A theoretical foundation of network localization and navigation," *Proc. IEEE*, vol. 106, no. 7, pp. 1136–1165, Jul. 2018.

[2] W. Zhao, J. Panerati, and A. P. Schoellig, "Learning-based bias correction for time difference of arrival ultra-wideband localization of resource-constrained mobile robots," *IEEE Robot. Autom. Lett.*, vol. 6, no. 2, pp. 3639–3646, Mar. 2021.

[3] Z. Zhang, H. Zhao, J. Wang, and Y. Shen, "Signal-multiplexing ranging for network localization," *IEEE Trans. Wireless Commun.*, vol. 21, no. 3, pp. 1694–1709, Mar. 2022.

[4] A. Conti, M. Guerra, D. Dardari, N. Decarli, and M. Z. Win, "Network experimentation for cooperative localization," *IEEE J. Sel. Areas Commun.*, vol. 30, no. 2, pp. 467–475, Feb. 2012.

[5] Y. Shen and M. Z. Win, "Fundamental limits of wideband localization – Part I: A general framework," *IEEE Trans. Inf. Theory*, vol. 56, no. 10, pp. 4956–4980, Oct. 2010.

[6] J. Cano, S. Chidami, and J. LeNy, "A kalman filter-based algorithm for simultaneous time synchronization and localization in uwb networks," in *Proc. IEEE Int. Conf. Robot. Autom.*, Montreal, QC, Canada, May 2019, pp. 1431–1437.

[7] T. Wang, K. Hu, Z. Li, K. Lin, J. Wang, and Y. Shen, "A semi-supervised learning approach for UWB ranging error mitigation," *IEEE Wireless Commun. Lett.*, vol. 10, no. 3, pp. 688–691, Mar. 2021.

[8] H. Wymeersch, S. Marano, W. M. Gifford, and M. Z. Win, "A machine learning approach to ranging error mitigation for uwb localization," *IEEE Trans. Commun.*, vol. 60, no. 6, pp. 1719–1728, Jun. 2012.

[9] J. Tiemann, J. Pillmann, and C. Wietfeld, "Ultra-wideband antenna-induced error prediction using deep learning on channel response data," in *Proc. IEEE Semiannual Veh. Technol. Conf.*, Sydney, NSW, Australia, Jun. 2017, pp. 1–5.

[10] J. Cano, G. Pagès, Éric Chaumette, and J. LeNy, "Clock and Power-Induced Bias Correction for UWB Time-of-Flight Measurements," *IEEE Robot. Autom. Lett.*, vol. 7, no. 2, pp. 2431–2438, Apr. 2022.

[11] M. A. Shalaby, C. C. Cossette, J. R. Forbes, and J. L. Ny, "Calibration and uncertainty characterization for ultra-wideband two-way-ranging measurements," in *Proc. IEEE Int. Conf. Robot. Autom.*, London, United Kingdom, Jun. 2023, pp. 4128–4134.

[12] *Decawave*, "DW1000 user manual, V2.18," 2017, [Online]. Available: https://www.decawave.com/dw1000/usermanual/.

[13] Y.-C. Wu, Q. Chaudhari, and E. Serpedin, "Clock synchronization of wireless sensor networks," *IEEE Signal Process. Mag.*, vol. 28, no. 1, pp. 124–138, Jan. 2011.

[14] D. Neirynck, E. Luk, and M. McLaughlin, "An alternative double-sided two-way ranging method," in *Proc. Workshop Positioning, Navigat. Commun.*, Bremen, Germany, Oct. 2016, pp. 1–4.

[15] H. Zhao, Z. Zhang, L. Xu, Y. Wang, and Y. Shen, "Enhancing timeliness in asynchronous vehicle localization: A signal-multiplexing network measuring approach," *IEEE Trans. Intell. Transp. Syst.*, pp. 1–15, 2024.

[16] A. D. Preter, G. Goysens, J. Anthonis, J. Swevers, and G. Pipeleers, "Range bias modeling and autocalibration of an uwb positioning system," in *Proc. Int. Conf. Indoor Positioning Indoor Navigat.*, Pisa, Italy, Sep. 2019, pp. 1–8.

[17] A. Ledergerber and R. D'Andrea, "Ultra-wideband range measurement model with gaussian processes," in *Proc. IEEE Conf. Control Technol. Appl.*, Maui, HI, USA, Aug. 2017, pp. 1929–1934.

[18] A. Ledergerber and R. D'andrea, "Calibrating away inaccuracies in ultra wideband range measurements: A maximum likelihood approach," *IEEE Access*, vol. 6, pp. 78 719–78 730, Dec. 2018.

[19] C. D. Franco, A. Prorok, N. Atanasov, B. Kempke, P. Dutta, V. Kumar, and G. J. Pappas, "Calibration-free network localization using non-line-of-sight ultra-wideband measurements," in *Proc. IEEE Inform. Processing in Sensor Networks*, Pittsburgh, PA, USA, Apr. 2017, pp. 235–246.

[20] Y. Li, S. Mazuelas, and Y. Shen, "A semi-supervised learning approach for ranging error mitigation based on UWB waveform," in *Proc. Military Commun. Conf.*, San Diego, United States, Nov. 2021, pp. 1–6.

[21] J. Hensman, A. Matthews, and Z. Ghahramani, "Scalable Variational Gaussian Process Classification," in *Proc. Int. Conf. on Artificial Intelligence and Statistics*, vol. 38, San Diego, California, USA, May 2015, pp. 351–360.

[22] J. Quinonero-Candela and C. E. Rasmussen, "A unifying view of sparse approximate gaussian process regression," *J. Mach. Learn. Res.*, vol. 6, pp. 1939–1959, Dec. 2005.

[23] J. Hensman, N. Fusi, and N. D. Lawrence, "Gaussian processes for big data," in *Proceedings of the Twenty-Ninth Conference on Uncertainty in Artificial Intelligence*. Arlington, Virginia, USA: AUAI Press, 2013, p. 282–290.

[24] H. Liu, Y.-S. Ong, and J. Cai, "Large-scale heteroscedastic regression via gaussian process," *IEEE Trans. Neural Netw. Learn. Syst.*, vol. 32, no. 2, pp. 708–721, Feb. 2021.

[25] *LUSTER LightTech Co., Ltd.*, "FZMotion Mocap System," [Online]. https://www.luster3ds.com/.